Photoreduction Mechanism of CO_2 to CO Catalyzed by a Three Component Hybrid Construct with a Bimetallic Rhenium Catalyst

Fei Wang,[†] Ronny Neumann,[‡] Coen de Graaf, [†,§]* Josep M. Poblet[†]*

[†] Department de Química Física i Inorgànica, Universitat Rovira i Virgili, Marcel·lí Domingo 1, 43007 Tarragona, Spain.

[‡] Department of Organic Chemistry, Weizmann Institute of Science, Rehovot 76100, Israel.

[§] ICREA, Passeig Lluis Companys 23, 08010, Barcelona, Spain.

KEYWORDS: Polyoxometalates, rhenium, graphitic carbon nitride, hybrid complexes, CO_2 photoreduction, hydrocarbon dehydrogenation, DFT

ABSTRACT: The mechanism of the photochemical reduction of carbon dioxide to carbon monoxide coupled to hydrocarbon dehydrogenation catalyzed by a three-component hybrid construct has been studied by combining DFT and CASSCF/CASPT2 calculations. The electron and proton coupled transfer mechanism is summarized as follows. Graphitic carbon nitride (g-CN), as the photosensitive semiconductor, absorbs visible blue light and transfers electrons to the polyoxometalate (POM), a process that is driven by the relative energy of the LUMO levels of the two species. Then, the hydrocarbon substrate (cyclohexene or cyclohexadiene) is dehydrogenated by the effect of holes formed during the photoexcitation of g-CN, which leads to the transfer of electrons to the oxidized g-CN and protons to the reduced POM. Under red light irradiation, the reduced POM transfers two electrons to the bimetallic Re(I) CO_2 reduction catalyst ([Re^1(bipyNNH$_2$)(CO)$_3$Cl−Re^2(bipy)(CO)$_3$Cl], bipy = 2,2'-bipyridine). The activated catalyst reduces CO_2 to CO while the proton-rich POM transfers two protons to generate the reduction co-product, H_2O. Acting as an electron/proton switch, the POM promotes hydrocarbon dehydrogenation by increasing the electron/hole separation upon photoactivation of g-CN and facilitates the transfer of electrons and protons to the Re catalyst for CO_2 reduction. The first electron transfer to the Re-complex is to the bipyNNH$_2$ ligand. The unpaired electron is then transferred to the Re-5dz^2 orbital, activating the coordination of CO_2. The combination of a strong interaction between the nearly degenerate d-π* orbitals of Re and the bipyNNH$_2$ ligand, the low reduction potential of -0.85 V and an extremely low free energy barrier of +2.4 kcal mol^{-1} for CO_2 ligation makes the bimetallic Re compound one of the best catalysts for transforming CO_2 to CO.

1. INTRODUCTION

The photoreduction of CO_2 using solar energy into valuable chemicals and especially more energy-dense organic compounds such as CO, HCOOH, CH_3OH, and CH_4 among others is regarded as a promising but challenging strategy to lessen our dependence on fossil fuels and guarantee sustainable energy development.[1] In this respect, for decades chemists have dedicated research to the establishment of synthetic catalytic systems for the CO_2 photochemical reduction in a laboratory setting, as summarized in a series of recent reviews.[2] According to those reviews, transition-metal compounds capable of photochemically catalyzing CO_2 reduction have been actively sought.[1a, 3] Of those compounds that can catalyze the reduction of CO_2 to CO, *fac*-Re(bipy)(CO)$_3$Cl (bipy = 2,2′-bipyridine) and its analogs have been proven to be superior to the majority others with regard to rates, selectivity, as well as catalyst lifetime.[4] These reduction reactions are usually carried out in organic solvents such as dimethylformamide or acetonitrile with or without an explicit extrinsic proton source. By adjusting the substituents at the 4,4′-positions of the bipy ligand, the reduction potential of the Re(I)-catalysts can be easily manipulated and a variety of substitutents have been shown to modulate activity.[5] Simple experimental operating conditions and easy-to-control reduction potentials make Re(I)-catalysts very promising candidates for industrial CO_2 photoreduction.

Although in some single-component photocatalytic systems, the photo absorber and the catalyst are the same compound,[6] the two processes of light absorption and catalysis are more often implemented by different components in a hybrid material.[7] Such hybrid constructs are usually composed of two parts with different functions: a photosensitizing agent and a CO_2 reduction catalyst. Upon light absorption, there is a one- or two-electron transfer from the photosensitizing agent to the catalyst, enabling the coordination of CO_2 and its subsequent reduction. Polyoxometalates (POMs) are a rather unique class of anionic metal oxide clusters formed by oxidation of d-block transition metal oxides, typically of W^{VI}, $Mo^{V,VI}$, or $VI^{V,V}$.[8] Due to their distinctive redox behavior where multiple electrons can be accepted and released while preserving their structural stability, POMs can regulate electron transfer pathways and thereby improve the activity and selectivity of catalytic

reactions.[4a-c, 8b, 9] Therefore, POMs are able to act as the relay of electron/protons associated with catalysts.[10] Related to this research, a series of hybrid systems consist of rhenium complexes and phosphotungstate, $[PW_{12}O_{40}]^{3-}$ were prepared and corresponding reaction mechanisms were reported for the photochemical reduction of CO_2 to CO incorporating the reduction and protonation of $[PW_{12}O_{40}]^{3-}$.[4a-c, 11] In another instance $[PW_{12}O_{40}]^{3-}$ transfer multiple electrons from the amino ligand of NH_2-MIL-53 to the Pt-catalyst driven by the irradiation and the hybrid material synergistically catalyze the H_2 evolution which proceeds on the platform of Pt nanoparticles.[12] Recently, a Ti-substituted polyoxotungstate embedded into the cavities of HKUST-1 together with Au nanoparticles was reported that it can promote photoreduction of CO_2 to CO and CH_4, acting as an electron/proton pond.[10d] All of these hybrid constructs demand photoexcited electron transfer from the photo absorber to the catalyst, which markedly affect the catalytic efficiency. Hence, the majorization of the electron transfer pathway is essential for efficient catalytic photoreduction.

Inspired by the above research background and considering that the transformation of CO_2 to CO is a two-electron redox reaction accompanied by the consumption of two protons to form H_2O, very recently, Neumann and coworkers proposed the first example of a CO_2 photochemical reduction reaction in the MeCN solvent coupled to a hydrocarbon dehydrogenation reaction catalyzed by a hybrid construct.[4a] A three-component construct (Figure 1) was reported that includes graphitic carbon nitride (g-CN) as a visible-light photosensitive semiconductor,[13] a phosphotungstate POM, $[PW_{12}O_{40}]^{3-}$, that behaves as an electron relay transferring electrons from the g-CN to a dimeric-rhenium-catalyst ($[Re^1(bipyNNH_2)(CO)_3Cl{-}Re^2(bipy)(CO)_3Cl]$, bipy = 2,2'-bipyridine) for CO_2 photoreduction. Upon photoactivation of g-CN, a cascade is initiated involving a hydrocarbon dehydrogenation coupled to the polyoxometalate reduction. Visible-light excites the reduced polyoxometalate to transfer electrons to the rhenium-based catalyst, enabling it to selectively reduce CO_2 to CO.

Based on this experimental research and previous computational investigation on Re(I)-based organometallic complexes,[4c] we used computational methods to validate the proposed mechanism for the hybrid system. To this end, we first established the two-electron transfer pathway between the three components and the photoreduction mechanism of CO_2 to CO by the bimetallic Re-catalyst. Next, in order to couple CO_2 reduction with hydrocarbon dehydrogenation, a multiple-proton transfer route accompanied by electron transfer is also proposed. Finally, we have analyzed the electronic properties of several Re(I) catalysts to explain why the bimetallic $[Re^1(bipyNNH_2)(CO)_3Cl{-}Re^2(bipy)(CO)_3Cl]$ is one of the best rhenium-based catalysts for transforming CO_2 to CO, as it combines a low reduction potential with a small energy barrier to reduce CO_2.

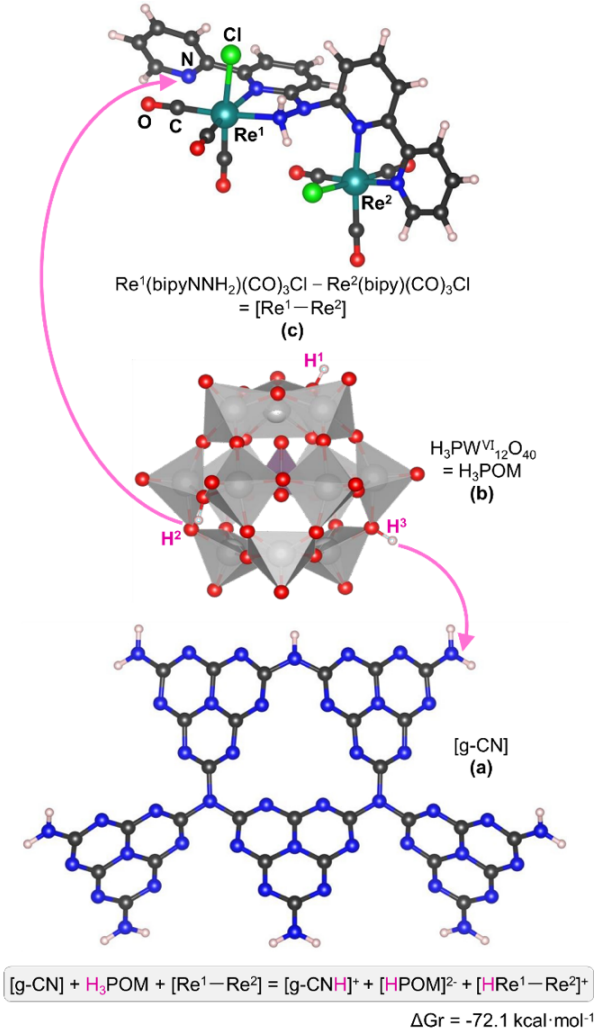

Figure 1. The structural representation of the hybrid {[g-CN] (a)/H_3POM(b)/$[Re^1{-}Re^2]$(c)} construct. The three components are attached to each other by acid-base interactions. The transfer of two protons from $H_3[PW_{12}O_{40}]$ to [g-CN] and to the catalyst $[Re^1{-}Re^2]$ is an exergonic process. Color code: C (dark gray), N (blue), O (red), Cl (green), W (light gray), Re (cyan), H (pink).

2. RESULTS AND DISCUSSION

2.1. The absorption spectra and energy balance between the three components of the hybrid construct. Initially, computations showed that the strong Brønsted acid $H_3PW_{12}O_{40}$ transfers one proton to a basic primary, terminal amine of g-CN and another proton to the Re-catalyst. The molecular electrostatic potential (MEP) map for $[Re^1\text{-}Re^2]$ demonstrates that the pyridine nitrogen is the most basic N site for protonation and the structure protonated at the pyridine nitrogen is more stable than the structure protonated at the amino nitrogen by 13.8 kcal mol^{-1}, which provides additional evidence that protonation is most likely to occur in pyridine nitrogen. Thus, another proton of the POM transfers to the pyridinyl nitrogen atom of the bipy ligand which is not coordinated to the Re(I) center, forming three charged components: $[g\text{-}CNH]^+$ (**1a**), $[HPW_{12}O_{40}]^{2-}$ (**1b**) and $[HRe^1{-}Re^2]^+$ (**1c**). These two proton transfer reactions combined are very exergonic, ΔG_r = -72.1 kcal mol^{-1}, as shown in Figure 1, enabling the formation of a very stable three-

component hybrid construct. The computed absorption spectra and corresponding frontier molecular orbitals at the B3LYP level of the various components are presented in Figure 2a and 2b. The simulated absorption spectrum of **1a** in blue shows that it mainly absorbs blue visible light with an absorption maximum at 360 nm. This corresponds to an electronic transition from HOMO-7 to LUMO. The energy of the latter is -3.05 eV, while the LUMO level of **1b** is -4.21 eV (Figure 2b). The large energy gap between the LUMO of **1a** and the LUMO of the POM (**1b**) provides a strong driving force for the transfer of an excited electron from **1a** to the LUMO of the POM (**1b**). The simulated absorption spectrum of the reduced POM (**2b**) is depicted by the red line in Figure 2a. The peak maximum is at 750 nm, corresponding to the electronic transition from the SOMO to LUMO+5. The LUMO+5 lies at higher energy (-2.85 eV) than the LUMO of **1c** (-3.01 eV), making it possible to transfer electrons from the reduced POM to **1c**. Using this level of theory, both the simulated spectra, that is those of **1a** and reduced **1b**, were in good consistency with the experimental spectra.[4a] Overall, the use of g-CN and reduced POM as the photosensitizer enables the excitation energies to envelop a large area of the visible spectrum and thereby allows the absorption of a significant part of the solar spectrum.

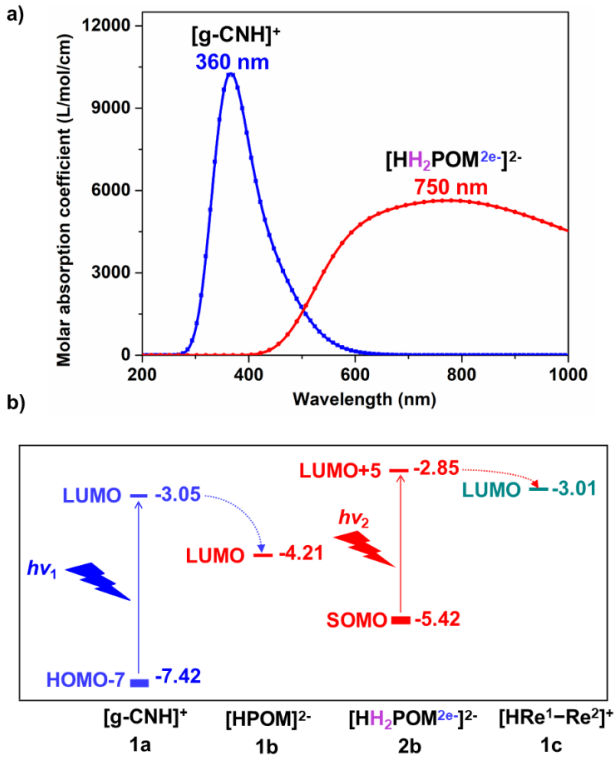

Figure 2. a) Simulated UV-vis-NIR spectra of $[g\text{-}CNH]^+$ (**1a**) in blue and reduced $[H_3POM^{2e}]^{2-}$ (**2b**) in red at the B3LYP level; b) Simplified molecular orbital energy diagram. The strongest light absorption corresponds to the transition of **1a** from HOMO-7 to LUMO, and from SOMO to LUMO+5 for reduced **2b**.

2.2. The central role of the POM as a shuttle for electrons and protons. Figure 3 schematizes the overall electron and proton transfer process. Excited by blue light, **1a** generates two higher-energy electrons with co-formation of two-electron oxidized **2a** (blue cycle). The hydrocarbon, for example, cyclohexene (C_6H_{10}) is hole oxidized to yield $[C_6H_{10}]^{2+}$ with the transfer of two electrons to **2a** and recovery of **1a**. **1b** can accept two photoexcited electrons from **1a** and two protons from intermediate $[C_6H_{10}]^{2+}$ generating two-electron reduced **2b**, where the two extra electrons are distributed on the W atoms of the POM (red cycle). After absorbing red light, **2b** acts as multiple electrons and protons donor transferring them to the Re catalyst for CO_2 reduction (green cycle). The two-electron/two-proton transfer process is an exothermic reaction with a substantial negative ΔG_r = -3.86 eV (the computational details are described in Figure S6). The transfer of the two protons is considered to be a single-step process, because the hypothetical intermediate involving a loss of a single proton, $[C_6H_9]$, is a highly unstable radical, which requires free energy about +12 eV, obviously unreachable at room temperature. Irradiation by red light excites the reduced-**2b** leading to the transfer of two electrons to **1c**, thereby activating the rhenium-based photoreduction catalyst. In the following subsections, we will add more details to the description of the mechanism.

This discussion of the overall process shows that the POM, acting as the electron/proton switch, promotes hydrocarbon dehydrogenation by boosting the electron/hole separation and facilitates the transfer of electrons and protons to the Re-based catalytic CO_2-reduction system. Other divalent anionic POM systems, such as $[SW_{12}O_{40}]^{2-}$, $[H_2SiW_{12}O_{40}]^{2-}$, $[H_4CoW_{12}O_{40}]^{2-}$, $[H_4P_2W_{18}O_{62}]^{2-}$, $[Mo_6O_{19}]^{2-}$ and $[HPMo_{12}O_{40}]^{2-}$ were studied, and we observed that the Keggin polyoxotungstates exhibit probably the optimal electronic structure to act as electrons and protons shuttle between **1a** and **1c**. While the LUMO levels for the Keggin polyoxotungstate anions depend not too much on the central ion, the Dawson polyoxotungstate, $[H_4P_2W_{18}O_{62}]^{2-}$ and the polyoxomolybdate, $[Mo_6O_{19}]^{2-}$ and $[HPMo_{12}O_{40}]^{2-}$ anions would not be appropriate carriers because their LUMOs would be too low or too high (Figure S4).

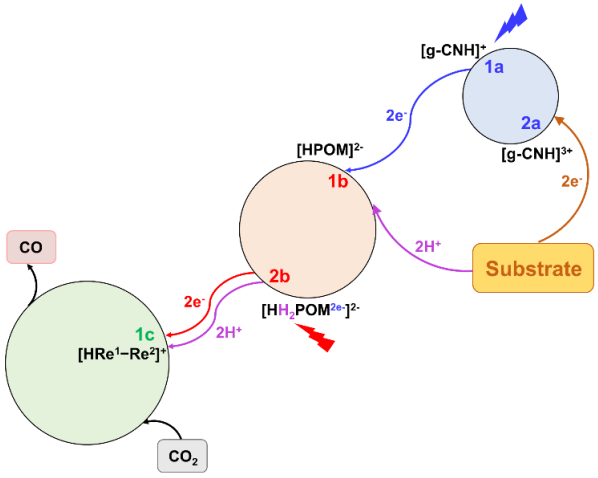

Figure 3. Schematic general view of the mechanism for the coupling CO_2 photoreduction and dehydrogenation of the substrate catalyzed by the hybrid $[g\text{-}CNH]^+$(**1a**)/$[HPOM]^{2-}$ (**1b**)/$[HRe^1{-}Re^2]^+$(**1c**) system.

2.3. Details of the catalytic cycle. We then carried out a detailed analysis of the CO_2 reduction catalyzed by $[HRe^1Cl{-}Re^2Cl]^+$, 1c. According to the known photochemistry of rhenium-based bipyridine complexes, a ligand, typically CO or Cl^-, can be eliminated by UV-blue light irradiation giving a solvent molecule such as MeCN the opportunity to occupy the created vacancy.[14] In this case, the rhenium catalyst is not symmetrical, that is, Re^1 is bound to one pyridinyl moiety and the bridging hydrazinyl group, while Re^2 is bound to two

pyridinyl moieties. The peak maximum of the simulated absorption spectrum of $[HRe^1Cl{-}Re^2Cl]^+$ is located at 300 nm and the corresponding transition is from σ orbitals between Re and Cl to π* orbitals of the bipy ligands, as shown in Figure S5. Hence, blue light irradiation could in principle de-chlorinate both rhenium centers, thereby allowing coordination of CO_2. However, the calculations show that the reaction Gibbs free energy (ΔG_r) and activation barrier ($\Delta G_r^{\ddagger}$) for CO_2 addition to Re^2 are +16.8 kcal mol^{-1} and ~ +20 kcal mol^{-1}, respectively, while for CO_2 addition to Re^1 they are only +0.7 kcal mol^{-1} and +2.4 kcal mol^{-1}, respectively. These values clearly indicate that Re^1 is the preferred catalytic center. Catalysis at the Re^1 site will be the focus of the further study of the CO_2 reduction mechanism. Reasons for the different catalytic reactivity at Re^1 and Re^2 will also be analyzed below.

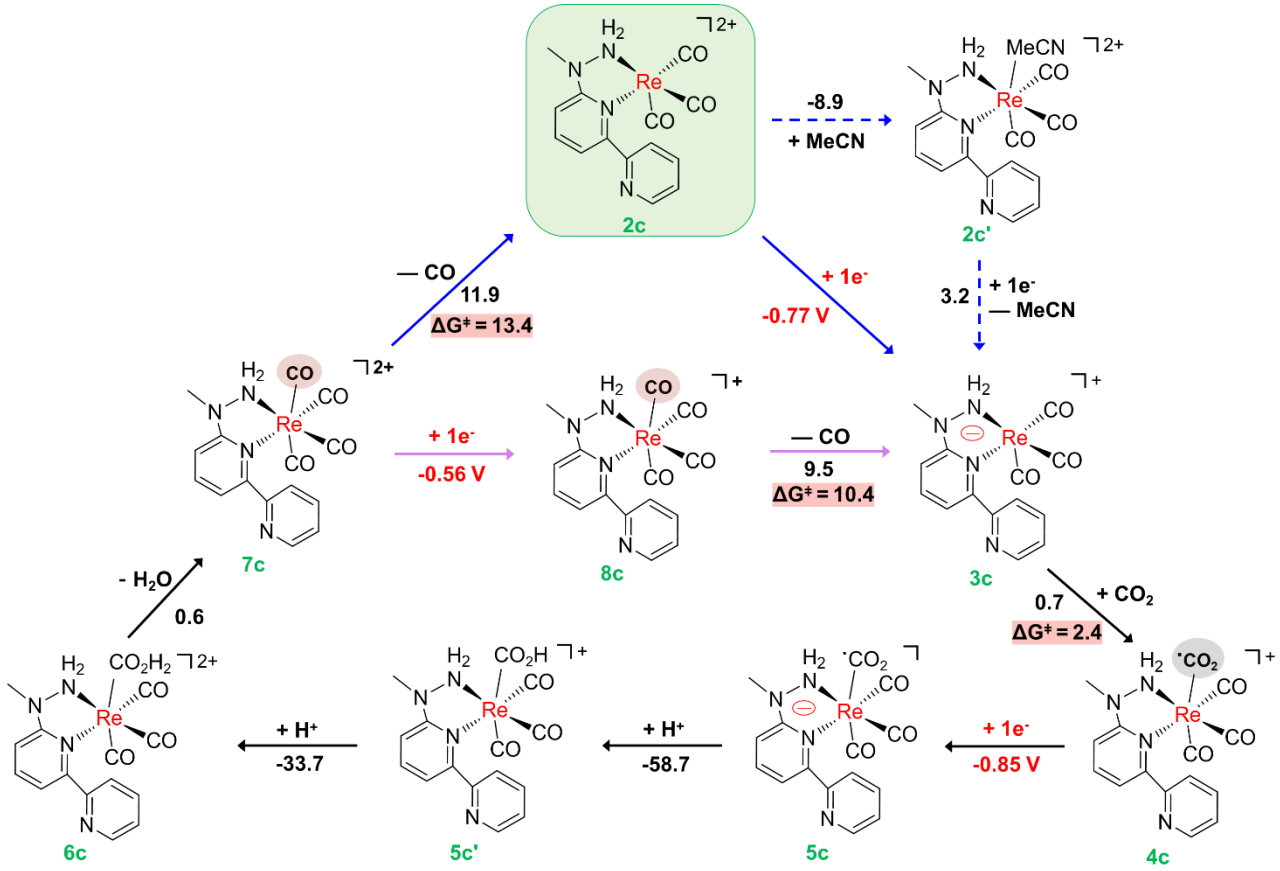

Figure 4. Reaction free energies and activation barriers (in kcal mol^{-1}) for the catalytic cycle. Only ligands of the active Re^1 center are shown for clarity. In all the species represented, the Re center acts as a Re(I) since the 1e-reduction of **2c** and **4c** leads to **3c** and **5c** with the additional electron being delocalized over the bipyNNH_2 ligand. The coordination of CO_2 and protonation on the ligand promote the electron transfer to the metal center from the organic ligand (see text). The potential addition and elimination steps of MeCN (**2c** → **2c'** → **3c**) are shown in dotted arrow lines. Energies associated with **5c** → **5c'** → **6c** steps are obtained considering that the protons are transferred from H_2POM and HPOM, respectively.

The ΔG_r and $\Delta G_r^{\ddagger}$ of the reaction steps associated with the catalytic cycle are summarized in Figure 4. After the elimination of Cl^- to yield **2c**, the solvent molecule MeCN is likely coordinated in an actually photoactivated ligand exchange reaction step giving **2c'**. The binding energy of MeCN to Re^1 is -19.5 kcal mol^{-1} and ΔG_r of this reaction is -8.9 kcal mol^{-1}. The elimination of MeCN requires a free energy of +3.2 kcal mol^{-1} with reduction of the Re^1 center. Although the addition and elimination of MeCN are thermodynamically favorable, as shown by the dotted arrow line (**2c** → **2c'** → **3c**) in Figure 4, the reaction is not necessarily faster than the electron transfer from the POMs (**2c** → **3c**). After one-electron transfer to **2c** (or **2c'**), **3c** with a 5-coordinated Re center is generated, in which the spin density is largely localized on the bipyNNH_2 ligand. Only a small fraction of the spin density is found on the coordinatively unsaturated Re center while the three CO ligands have negligible spin populations (Figure 5). Hence, **3c** is considered as a [Re(I)−bipyNNH_2(1-)] compound as opposed to a [Re(0)−bipyNNH_2(0)] intermediate. This is consistent with previous spectroscopic evidence that demonstrated a shift of about 21 cm^{-1} in the high-energy band that was attributed to the formation of a bipy radical.[5i] Whereas the d-orbitals of first-row transition metal ions are relatively tightly bound to the nucleii and display a low orbital energy, the 5d orbitals of the Re atom are more diffuse and higher in energy. Thus, the bipy π* orbital is predicted to be lower in energy than the Re $5dz^2$ orbital. The initial formation of [Re(I) −bipyNNH_2(1-)] indeed shows that the first one-electron reduction is at the bipyNNH_2 ligand. This is also supported by experimental observations that the reduction potential of the Re(I)-catalyst can be manipulated by adjusting the substituents at the 4,4′-positions of the bipy ligand (see section 2.4).

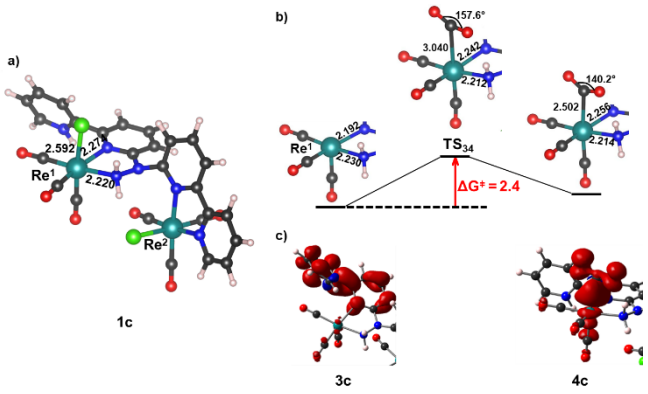

Figure 5. Structure of **1c** (a), free energy profile (b) and spin density distribution (c) for the CO_2 ligation steps. Since the single electron is only (de)localized over the ligands of Re^1 center in **2c**, only the atoms around the Re^1 center are shown in **3c**, **TS_{34}** and **4c**, where all atoms around of Re^2 are omitted for clarity.

Furthermore, complete active space self-consistent field (CASSCF) calculations were carried out to better understand the electron transfer in the process of CO_2 approaching the Re center. The CASSCF spin populations of the ground and first excited state as function of the distance between Re and CO_2 and corresponding active orbitals are shown in Figure S7-8. The two active orbitals marked as "Re−CO_2 σ/π* bipyNNH_2" are the two orbitals that are singly occupied in the first two roots of the CASSCF calculation. A unitary transformation of these two orbitals leads to localized orbitals, either on the bipyNNH_2 ligand or on Re−CO_2. Because of the multiconfigurational character of the wave function, localized and delocalized descriptions are equivalent and, as can be seen in spin population plots, the lowest root has one unpaired electron on bipyNNH_2 ligand at a large distance, which is transferred to Re−CO_2 at a shorter distance. The low occupation of the $5dz^2$ orbital on Re^1 in **3c** facilitates the approach of CO_2 as there is initially no electron-electron repulsion between the ligand and Re. In a later stage, when the CO_2 is closer to the Re^1 center, the unpaired electron is transferred from bipyNNH_2 to the Re-$5dz^2$ orbital and the Re−C bond formation is initiated. Therefore, we postulate that the interaction between the bipyNNH_2 π* orbital and the Re^1 d orbitals and their succeeding occupations after reduction has a major impact on the CO_2 ligation, which is confirmed in the next section. The CASSCF calculated energy barrier for CO_2 coordination is much higher than the one predicted with the DFT calculation. This is not unexpected since the CASSCF wave function does not account for the so-called dynamic electron correlation. This effect is commonly included with second-order perturbation theory (CASPT2). Indeed, the corresponding potential energy surface depicted in Figure S9 (right) shows a barrier of the same order of magnitude as the DFT barrier. The inversion of the stability of the [Re(I) −bipyNNH_2(1-)] and [Re(0)−bipyNNH_2(0)] electronic states occurs when the distance between Re and CO_2 is around 3.1 Å during the approach of CO_2 to Re.

The ligation of CO_2 to intermediate **3c** by forming a Re–C bond is a little bit endothermal by ~0.7 kcal mol^{-1} to generate **4c**. Figure 5 presents the free energy profile and structural changes for the CO_2 ligation, which shows that the activation barrier for the CO_2 coordination is only +2.4 kcal mol^{-1} where the Re−C bond is belike 3.0 Å and the O=C=O angle is about 158° in the transition state structure (**TS_{34}**), while the Re−C bond length is 2.5 Å and the O=C=O angle is 140° in intermediate, **4c**. This indicates that the interaction between Re center and CO_2 is stronger than in the previous studied Re-polyoxometalate hybrid construct, where the Re−C bond length is ~2.9 Å and the O=C=O angle ~165°.[4c]

When a second electron is transferred from the POM to the catalyst, the additional electron is also located on the bipyNNH_2 ligand of Re^1 center generating **5c** [Re(I) −bipyNNH_2(1-)]. Later, it is transferred to the Re^1 center, forming the [Re(0)−bipyNNH_2(0)] electronic state. The potential energy surface and structural changes for the second electron transfer and CO elimination are presented in Figure 6. The reduction does not significantly affect the Re−CO_2 bond. The O=C=O angle remains 140° and the Re−C distance is still ~2.5 Å. On the basis of previous experimental and computational investigation,[1a, 4d, 10b, 14b, 15] two subsequent protonation steps are demanded to generate CO. As presented in Figure 5c, the electron of the [Re^1(bipyNNH_2)$(CO)_3$(CO_2)] part in **4c** is largely distributed on the CO_2 ligand; which leads to a fractional negative charge on the CO_2 and promotes the first protonation of the bound CO_2 ligand to form a hydroxycarbonyl complex **5c'**, which is about 59 kcal mol^{-1} lower in energy. Previous computational research on Re-based catalytic systems has demonstrated that these protonation steps are barrier-free.[16] The protonation step weakens one of the C=O bonds and elongates it to 1.37 Å in **5c** from 1.22 Å in **5c'**, while the Re−C(COOH) bond is strengthened with the length decreasing considerably by 0.34 Å. Due to a fractional negative charge still on the COOH ligand in **5c'**, further protonation can occur, which leads to the cleavage of C−OH bond and the generation of H_2O and the cationic tetracarbonyl complex **6c**, releasing CO after photoreduction. This step is exothermal by about -34 kcal mol^{-1}, assuming the reduced POM to be the proton source. The departure of H_2O is a slightly endothermal process by 0.6 kcal mol^{-1} from **6c** to **7c**. At this point, there are two alternatives involving the removal of a CO and 1e-reduction step. As shown the blue path in Figure 4, the free energy barrier for the direct cleavage of the Re−CO bond of **7c** is not very high, +13.4 kcal mol^{-1}. Similar results (~12 kcal mol^{-1}) have been found in studies on related compounds.[16e] However, when CO is released from the previously reduced **7c**, the energy barrier is slightly lower, +10.4 kcal mol^{-1} (the purple path in Figure 4). Although this latter pathway is more favorable from the energy point of view, we can not rule out that both can occur simultaneously.

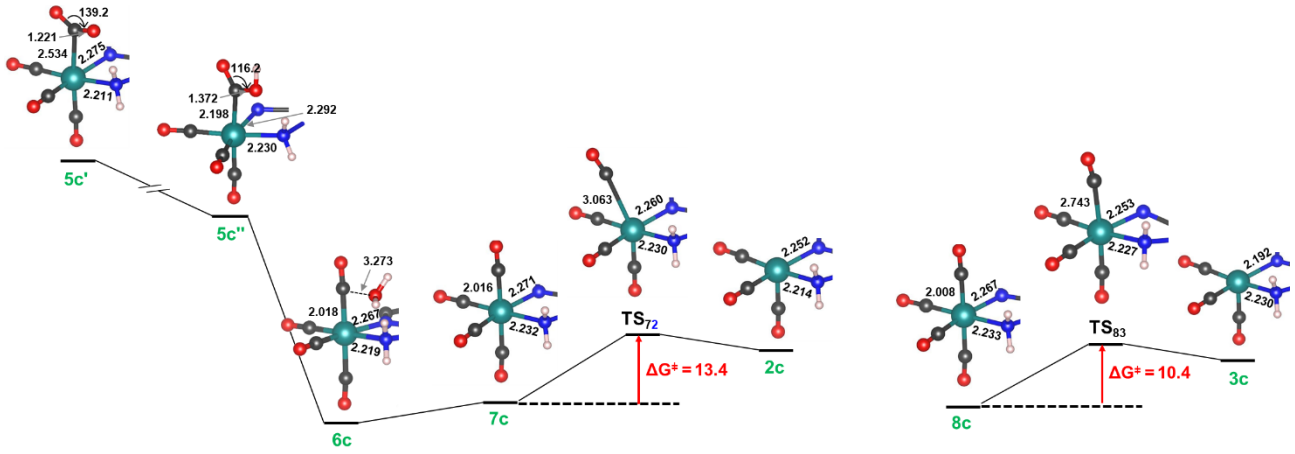

Figure 6. The schematic diagram for the potential energy surface of the second electron transfer and CO elimination. All distances are in Å and angles are in degrees and the free energy barriers are in kcal mol^{-1}. For other numerical values see Figure 4.

Chart 1. The comparison of the previously reported classical Re(I) catalysts (1-9) and the present work ([Re^1−Re^2])

Compound	Structure		DFT			Exp.
			LUMO[a]	ΔG‡[b]	V[c]	V[c]
1		R=H; R'=H	-2.49	+21.2	-1.34	-1.34[5i]
2	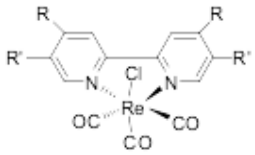	R=CH_3; R'=H	-2.39		-1.53	-1.43[5i]
3		R=*tBu*; R'=H	-2.34		-1.56	-1.45[5i]
4		R=OCH_3; R'=H	-2.19		-1.62	-1.49[5i]
5		R=OH; R'=H	-2.36		-1.55	-1.53[5b]
6		R=COOH; R'=H	-3.05	+10.6	-0.88	-0.94[5i]
7		R=H; R'=alkynyl	-2.89	+22.1	-0.99	-1.15[5d]
8	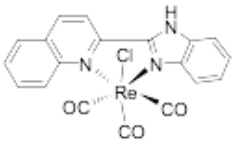		-2.16		-1.61	-1.54[5h]
9	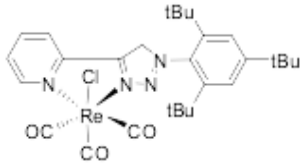		-2.12		-1.73	-1.70[5g]
[Re^1−Re^2]	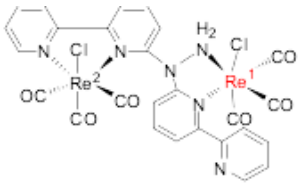		-3.01	+2.4	-0.77	-0.73[4a]

[a]in eV; [b]free energies barriers in kcal·mol^{-1}; [c]the first reduction potential in V (*vs* SHE).

2.4. Influence of substituents on the bipy ligand on the properties of the catalyst. The redox potential and the overall catalytic activity are significantly influenced by substituents on the bipy ligand. As shown in Chart 1, the experimental reduction potentials of a series of Re(I)-catalysts ranging from -0.73 V to -1.70 V, are nicely reproduced by our present DFT calculations. Unlike the previously studied monometallic-Re(I) catalysts (**1**-**9**), the catalyst analyzed here contains two Re(I) centers, one Re^2 center has the classical $[Re^2(bipy)(CO)_3Cl]$ coordination where both sp^2 N-atoms of the bipy ligand are ligated to the metal while the other Re center, Re^1, $[Re^1(bipyNNH_2)(CO)_3Cl]$, has a less conventional coordination sphere with only one Re−N(bipy) bond and a second Re^1–N bond with the NNH_2 ligand with a sp^3 hybridization (see Chart 1 for a schematic view of the structure). The main consequence of this non-symmetric coordination is that the LUMO of the bimetallic catalyst is localized on the $bipyNNH_2$ ligand of the Re^1 center, with a lower energy than most of the other rhenium compounds reported in Chart 1. Therefore, the spin density of the bimetallic catalyst after one-electron reduction **3c** is also localized on the $bipyNNH_2$ ligand of Re^1. This confirms again that the CO_2 reduction occurs at the Re^1 center. In fact, if we replace the entire $Re^2bipy(CO)_3Cl$ moiety with a methyl group, the properties of the catalyst (summarized in Table S1, $[Re^1-CH_3]$) change only marginally compared to the bimetallic $[Re^1-Re^2]$ catalyst, supporting the conclusion that the Re^2 center does not play a direct role on the CO_2 reduction cycle. Among the compounds examined in Chart 1, **6** and **7** were of special note because of their low reduction potential, -0.88 V and -0.99 V, respectively. Compound **6** has two carboxyl groups at the 4,4 '-positions of the bipy ligand and compound **7** has two alkynyl groups at the 3,3'-positions of the bipy ligand. The difference between the two compounds lies in the $\Delta G_r^{\ddagger}$ for the CO_2 addition, which were computed to be +10.6 kcal mol^{-1} and +22.1 kcal mol^{-1}, respectively. The latter $\Delta G_r^{\ddagger}$ is very similar to the value computed for the parent compound with an unsubstituted bipy ligand, **1**. However, the carboxyl groups in **6** reduces $\Delta G_r^{\ddagger}$ by more than 10 kcal mol^{-1} with respect to **1**. These carboxylate electron-withdrawing groups reduce the energy of the Re-d and the bipy-π* orbitals. The stabilization is larger for the Re-d orbitals and the overall effect is a reduction of the gap between the bipy-π* and the Re-d orbitals from 0.85 eV in **1** to 0.46 eV in **6**. The smaller gap favors electron transfer from bipy to the Re atom explaining the lower $\Delta G_r^{\ddagger}$ for the CO_2 addition of **6**.

Compared to the aforementioned compounds, the Re^1 center in $[Re^1-Re^2]$ exhibits both a very low reduction potential (-0.85 V) and a very low $\Delta G_r^{\ddagger}$ (+2.4 kcal mol^{-1}) for the CO_2 addition. Thus, the bimetallic $[Re^1-Re^2]$ compound is expected to be a superior catalyst for the reduction of CO_2 to CO. By exchanging one N (sp^2) coordination site with a sp^3 hybridized N atom, the σ donating character of the coordination sphere is reduced. This significantly lowers the ligand-field exerted on the metal and stabilizes the Re-d orbitals in comparison to the classical symmetric bidentate bipy coordination complexes. The d-π* orbital energy gap is further reduced, leading to an extremely low $\Delta G_r^{\ddagger}$ for CO_2 addition. Specifically, the energy gap in **6** of 0.46 eV is reduced to almost 0 eV, allowing a strong interaction between the Re^1 center and the $bipyNNH_2$ ligand. The frontier molecular orbitals, Figure S10, show that the Re-d orbitals and the bipy-π* orbital are completely separated in compounds **1** and **6**, while $[Re^1-Re^2]$ shows nearly degenerate d-π* orbitals of Re and the $bipyNNH_2$ ligand. Therefore, when CO_2 approaches Re^1, the electrons on the $bipyNNH_2$ ligand can be easily transferred to Re^1 to interact with CO_2 without any barrier, very significantly reducing the $\Delta G_r^{\ddagger}$ for CO_2 addition. These results confirm our previous hypothesis based on CASSCF calculations that the CO_2 additive affinity is mainly influenced by the energy gap between the bipy π* orbital and the Re d orbitals and the succeeding occupations after reduction.

3. CONCLUSIONS

In summary, a detailed computational study has been accomplished for the mechanism of the photochemical reduction of CO_2 to CO coupled to hydrocarbon dehydrogenation catalyzed by a three components of hybrid construct, $\{[g\text{-}CN]-POM-[Re^1-Re^2]\}$. We first rationalize the electron/proton transfer pathway between the three components. After absorbing blue light, [g-CN] transfers two electrons to the polyoxometalate (POM), which is driven by a large LUMO energy difference between the two compounds. Then, the hydrocarbon, transfers two electrons to the holes of oxidized g-CN and two (or even more) protons to the reduced POM, leading to the dehydrogenation of the hydrocarbon. The transfer of the two protons is considered as a single-step process with the formation of $[C_6H_8]$, skipping the highly unstable radical $[C_6H_9]$ due to the loss of a single proton. Next, the reduced POM is excited by red light and then transfers two electrons to Re(I) species. Finally, the activated catalyst captures and reduces CO_2 and in the process the hydrogen-rich POM transfers two protons to the CO_2-coordinated Re-species to generate the reduction products, CO and water. Throughout the process, the POM is crucial. On the one hand, it acts as an electron acceptor to facilitate electron-hole separation, and on the other hand, it serves as an electron donor to a Re-based CO_2 catalytic reduction system. By studying the catalytically photochemical reduction cycle of CO_2 to CO by the Re(I)-catalyst, the formation of the species $[Re^1(I)-bipyNNH_2(1\text{-})]$ indicates that it is a ligand-based reduction instead of a metal-based reduction and thus the $bipyNNH_2$ ligand is responsible for the first reduction potential. Moreover, the energy gap between the $bipyNNH_2$ π* orbital and the Re dz^2 orbitals and the succeeding occupations after reduction is predicted to be the main reason of the CO_2 binding affinity. The particular environment of Re^1 in the bimetallic complex, $[Re^1-Re^2]$ makes this catalyst exceptional, with a very low reduction potential and high affinity for CO_2 coordination after its reduction.

COMPUTATIONAL DETAILS.

All DFT calculations were performed by employing the Gaussian 16 A.03 program package.[17] The geometries were optimized by the hybrid B3LYP exchange-correlation functional.[18] The LanL2DZ effective core potential (ECP) basis set[19] commonly used for Re complexes[4c, 5a, 20] was applied for Cl, W and Re atoms, while the 6-31G(d,p) basis set[21] was applied for the remaining H, C, O, and N atoms. Vibrational frequency calculations were carried out at 298.15 K and 1 atm using the same level of theory as for the geometry optimizations for all intermediates to confirm that those geometries locate at the lowest point of the potential energy surface. The single imaginary frequency of the transition state structure is related to the normal mode of vibration linking reactants and products. The visible absorption spectra were acquired through TDDFT calculations.[22] The M06,[23] O3LYP,[24] and

CAM-B3LYP[25] functionals were applied to calculate the spectra. The solvent MeCN effect (ε = 36.6, refractive index = 1.334) was included adopting the IEF-PCM solvent model.[26]

The CASSCF/CASPT2 calculations were done with the OpenMolcas code.[27] Single point calculations were carried out on DFT optimized structures, restricting the Re-CO_2 distance. The basis sets taken from the ANO-RCC internal library, which contains basis sets optimized for scalar relativistic corrections and semi-core valence electron correlation.[28] The following contractions of the primitive set of functions were used: Re(7s,6p,5d,2f,1g); C, N, O (4s,3p,1d) and H (2s,1p). The active space contained 13 electrons distributed in all possible ways over 13 active orbitals (see Figure. S6). A state-average optimization of the energy over the lowest eight doublets was performed to ensure that the active orbitals keep their character along the whole potential energy surface.

In order to compare with other reported compounds, we also calculated the reduction potential of POMs and Re-catalysts involved in the current work by computing the free energy associated with the process. The reduction potentials were obtained using the formula $E = \frac{-\Delta G_{ox \vee red}}{F}$, where $\Delta G_{ox|red}$ is the free energy change of the reduction process. E_{abs} = -4.24 V was taken as the absolute standard potential of this half reaction, $½H_2(g) \rightarrow H^+(aq) + 1e^-$.[29] A data set collection of computational results is available in the ioChem-BD repository and can be accessed via ttps://doi.org/10.19061/iochem-bd-2-46.[30]

AUTHOR INFORMATION

Corresponding Author

*E-mail: coen.degraaf@urv.cat
*E-mail: josepmaria.poblet@urv.cat

ORCID

Josep M. Poblet: 0000-0002-4533-0623
Coen de Graaf: 0000-0001-8114-6658
Fei Wang: 0000-0001-5106-5793
Ronny Neumann: 0000-0002-5530-1287

Notes

The authors declare no competing financial interest.

ASSOCIATED CONTENT

Supporting Information

The Supporting Information is available free of charge on the ACS Publications website.
Simulated visible spectra; energy balance and computational details of the ΔG_r associated to the protons transfer; CASSCF spin populations and active orbitals; relative CASPT2 and MS-CASPT2 energies of the ground and first excited state; the comparison of the bimetallic [Re^1−Re^2] and monometallic [Re^1−CH_3] and some frontier molecular orbitals.

ACKNOWLEDGMENT

This project has received funding from the European Union's Horizon 2020 research and innovation program under the Marie Skłodowska-Curie grant agreement No. 713679 and from the Universitat Rovira i Virgili (URV). J.M.P. and C.d.G thank the Spanish Ministry of Science (grants CTQ2017-87269-P and CTQ2017-83566-P) and the Generalitat de Catalunya (grant 2017SGR629) for support. J.M.P. also thanks ICREA foundation for an ICREA ACADEMIA award. R. N. thanks the Minerva Foundation for support with funding from the Federal German Ministry for Education and Research. R.N. is the Rebecca and Israel Sieff Professor of Organic Chemistry.

REFERENCES

1. a) Liang, H.-P.; Acharjya, A.; Anito, D. A.; Vogl, S.; Wang, T.-X.; Thomas, A.; Han, B.-H. Rhenium-metalated Polypyridine-based Porous Polycarbazoles for Visible-light CO_2 Photoreduction. *ACS Catal.* **2019,** *9*, 3959-3968; b) Sun, Z.; Talreja, N.; Tao, H.; Texter, J.; Muhler, M.; Strunk, J.; Chen, J. Catalysis of Carbon Dioxide Photoreduction on Nanosheets: Fundamentals and Challenges. *Angew. Chem. Int. Ed.* **2018,** *57*, 7610-7627; c) Khalil, M.; Gunlazuardi, J.; Ivandini, T. A.; Umar, A. Photocatalytic Conversion of CO_2 Using Earth-abundant Catalysts: a Review on Mechanism and Catalytic Performance. *Renew. Sust. Energ. Rev.* **2019,** *113*, 109246; d) Fu, J.; Liu, K.; Jiang, K.; Li, H.; An, P.; Li, W.; Zhang, N.; Li, H.; Xu, X.; Zhou, H.; Tang, D.; Wang, X.; Qiu, X.; Liu, M. Graphitic Carbon Nitride with Dopant Induced Charge Localization for Enhanced Photoreduction of CO_2 to CH_4. *Adv. Sci.* **2019,** *6*, 1900796; e) Ye, L.; Wang, H.; Jin, X.; Su, Y.; Wang, D.; Xie, H.; Liu, X.; Liu, X. Synthesis of Olive-green Few-layered BiOI for Efficient Photoreduction of CO_2 into Solar Fuels under Visible/near-infrared Light. *Sol. Energy Mater. Sol. Cells* **2016,** *144*, 732-739.
2. a) Thompson, W. A.; Sanchez Fernandez, E.; Maroto-Valer, M. M. Review and Analysis of CO_2 Photoreduction Kinetics. *ACS Sustain. Chem. Eng.* **2020,** *8*, 4677-4692; b) Li, X.; Yu, J.; Jaroniec, M.; Chen, X. Cocatalysts for Selective Photoreduction of CO_2 into Solar Fuels. *Chem. Rev.* **2019,** *119*, 3962-4179; c) Wu, H.-L.; Li, X.-B.; Tung, C.-H.; Wu, L.-Z. Semiconductor Quantum Dots: an Emerging Candidate for CO_2 Photoreduction. *Adv. Mater.* **2019,** *31*, 1900709; d) Li, R.; Zhang, W.; Zhou, K. Metal-organic-framework-based Catalysts for Photoreduction of CO_2. *Adv. Mater.* **2018,** *30*, 1705512.
3. a) Feng, X.; Pi, Y.; Song, Y.; Brzezinski, C.; Xu, Z.; Li, Z.; Lin, W. Metal-organic Frameworks Significantly Enhance Photocatalytic Hydrogen Evolution and CO_2 Reduction with Earth-abundant Copper Photosensitizers. *J. Am. Chem. Soc.* **2020,** *142*, 690-695;b) Wang, X.-K.; Liu, J.; Zhang, L.; Dong, L.-Z.; Li, S.-L.; Kan, Y.-H.; Li, D.-S.; Lan, Y.-Q. Monometallic Catalytic Models Hosted in Stable Metal-organic Frameworks for Tunable CO_2 Photoreduction. *ACS Catal.* **2019,** *9*, 1726-1732; c) Todorova, T. K.; Huan, T. N.; Wang, X.; Agarwala, H.; Fontecave, M. Controlling Hydrogen Evolution during Photoreduction of CO_2 to Formic Acid Using $[Rh(R\text{-}bpy)(Cp^*)Cl]^+$ Catalysts: A Structure-activity Study. *Inorg. Chem.* **2019,** *58*, 6893-6903; d) Meier, A. J.; Garg, A.; Sutter, B.; Kuhn, J. N.; Bhethanabotla, V. R. MoS_2 Nanoflowers as a Gateway for Solar-driven CO_2 Photoreduction. *ACS Sustain. Chem. Eng.* **2019,** *7*, 265-275; e) Xie, Y.; Fang, Z.; Li, L.; Yang, H.; Liu, T.-F. Creating Chemisorption Sites for Enhanced CO_2 Photoreduction Activity through Alkylamine Modification of MIL-101-Cr. *ACS Appl. Mater. Interfaces* **2019,** *11*, 27017-27023; f) Chen, E.-X.; Qiu, M.; Zhang, Y.-F.; Zhu, Y.-S.; Liu, L.-Y.; Sun, Y.-Y.; Bu, X.; Zhang, J.; Lin, Q. Acid and Base Resistant Zirconium Polyphenolate-metalloporphyrin Scaffolds for Efficient CO_2 Photoreduction. *Adv. Mater.* **2018,** *30*, 1704388; g) Yan, Y.; Yu, Y.; Huang, S.; Yang, Y.; Yang, X.; Yin, S.; Cao, Y. Adjustment and Matching of Energy Band of TiO_2-based Photocatalysts by Metal Ions (Pd, Cu, Mn) for Photoreduction of CO_2 into CH_4. *J. Phys. Chem. C.* **2017,** *121*, 1089-1098.
4. a) Yu, H.; Haviv, E.; Neumann, R. Visible-light Photochemical Reduction of CO_2 to CO Coupled to Hydrocarbon Dehydrogenation. *Angew. Chem. Int. Ed.* **2020,** *59*, 6219-6223; b) Haviv, E.; Shimon, L. J. W.; Neumann, R. Photochemical Reduction of CO_2 with Visible Light Using a Polyoxometalate as Photoreductant. *Chemistry* **2017,** *23*, 92-95; c) Ci, C.; Carbó, J. J.; Neumann, R.; Graaf, C. d.; Poblet, J. M. Photoreduction Mechanism of CO_2 to CO Catalyzed by a Rhenium(I)-polyoxometalate Hybrid Compound. *ACS Catal.* **2016,** *6*, 6422-6428; d) Khenkin, A. M.; Efremenko, I.; Weiner, L.; Martin, J. M. L.; Neumann, R. Photochemical Reduction of Carbon Dioxide

Catalyzed by a Ruthenium-substituted Polyoxometalate. *Chem. Eur. J*. **2010,** *16*, 1356-1364.

5. a) Benson, E. E.; Sampson, M. D.; Grice, K. A.; Smieja, J. M.; Froehlich, J. D.; Friebel, D.; Keith, J. A.; Carter, E. A.; Nilsson, A.; Kubiak, C. P. The Electronic States of Rhenium Bipyridyl Electrocatalysts for CO_2 Reduction as Revealed by X-ray Absorption Spectroscopy and Computational Quantum Chemistry. *Angew. Chem. Int. Ed.* **2013,** *52*, 4841-4844; b) Manbeck, G. F.; Muckerman, J. T.; Szalda, D. J.; Himeda, Y.; Fujita, E. Push or Pull? Proton Responsive Ligand Effects in Rhenium Tricarbonyl CO_2 Reduction Catalysts. *J. Phys. Chem. B* **2015,** *119*, 7457-7466; c) Teesdale, J. J.; Pistner, A. J.; Yap, G. P.; Ma, Y. Z.; Lutterman, D. A.; Rosenthal, J. Reduction of CO_2 Using a Rhenium Bipyridine Complex Containing Ancillary BODIPY Moieties. *Catal. Today* **2014,** *225*, 149-157; d) Portenkirchner, E.; Gasiorowski, J.; Oppelt, K.; Schlager, S.; Schwarzinger, C.; Neugebauer, H.; Knor, G.; Sariciftci, N. S. Electrocatalytic Reduction of Carbon Dioxide to Carbon Monoxide by a Polymerized Film of an Alkynyl-substituted Rhenium(I) Complex. *ChemCatChem* **2013,** *5*, 1790-1796; e) Qiao, X.; Li, Q.; Schaugaard, R. N.; Noffke, B. W.; Liu, Y.; Li, D.; Liu, L.; Raghavachari, K.; Li, L.-S. Well-defined Nanographene-rhenium Complex as an Efficient Electrocatalyst and Photocatalyst for Selective CO_2 Reduction. *J. Am. Chem. Soc*. **2017,** *139*, 3934-3937; f) Andrade, G. A.; Pistner, A. J.; Yap, G. P.; Lutterman, D. A.; Rosenthal, J. Photocatalytic Conversion of CO_2 to CO Using Rhenium Bipyridine Platforms Containing Ancillary Phenyl or BODIPY Moieties. *ACS Catal* **2013,** *3*, 1685-1692; g) Ching, H. Y.; Wang, X.; He, M.; Perujo Holland, N.; Guillot, R.; Slim, C.; Griveau, S.; Bertrand, H. C.; Policar, C.; Bedioui, F.; Fontecave, M. Rhenium Complexes Based on 2-Pyridyl-1,2,3-triazole Ligands: a New Class of CO_2 Reduction Catalysts. *Inorg. Chem.* **2017,** *56*, 2966-2976; h) Sinha, S.; Berdichevsky, E. K.; Warren, J. J. Electrocatalytic CO_2 Reduction Using Rhenium(I) Complexes with Modified 2-(2′-pyridyl)imidazole Ligands. *Inorg. Chim. Acta* **2017,** *460*, 63-68; i) Smieja, J. M.; Kubiak, C. P. Re(bipy-tBu)$(CO)_3$Cl-improved Catalytic Activity for Reduction of Carbon Dioxide: IR-spectroelectrochemical and Mechanistic Studies. *Inorg. Chem.* **2010,** *49*, 9283-9289.
6. a) Hoch, L. B.; Wood, T. E.; O'Brien, P. G.; Liao, K.; Reyes, L. M.; Mims, C. A.; Ozin, G. A. The Rational Design of a Single-component Photocatalyst for Gas-phase CO_2 Reduction Using Both UV and Visible Light. *Adv. Sci*. **2014,** *1*, 1400013; b) Wu, J.; Huang, Y.; Ye, W.; Li, Y. CO_2 Reduction: from the Electrochemical to Photochemical Approach. *Adv. Sci.* **2017,** *4*, 1700194.
7. a) Lin, J.; Pan, Z.; Wang, X. Photochemical Reduction of CO_2 by Graphitic Carbon Nitride Polymers. *ACS Sustain. Chem. Eng.* **2014,** *2*, 353-358; b) Kuramochi, Y.; Ishitani, O. Iridium(III) 1-Phenylisoquinoline Complexes as a Photosensitizer for Photocatalytic CO_2 Reduction: a Mixed System with a Re(I) Catalyst and a Supramolecular Photocatalyst. *Inorg. Chem.* **2016,** *55*, 5702-5709.
8. a) Lopez, X.; Carbo, J. J.; Bo, C.; Poblet, J. M. Structure, Properties and Reactivity of Polyoxometalates: a Theoretical Perspective. *Chem. Soc. Rev.* **2012,** *41*, 7537-71; b) Blasco-Ahicart, M.; Soriano-López, J.; Carbó, J. J.; Poblet, J. M.; Galan-Mascaros, J. R. Polyoxometalate Electrocatalysts Based on Earth-abundant Metals for Efficient Water Oxidation in Acidic Media. *Nat. Chem.* **2018,** *10*, 24-30.
9. a) Lu, B.-B.; Yang, J.; Che, G.-B.; Pei, W.-Y.; Ma, J.-F. Highly Stable Copper(I)-based Metal–organic Framework Assembled with Resorcin[4]arene and Polyoxometalate for Efficient Heterogeneous Catalysis of Azide–alkyne "Click" Reaction. *ACS Appl. Mater. Interfaces* **2018,** *10*, 2628-2636; b) Su, X.-F.; Guan, W.; Yan, L.-K.; Su, Z.-M. Tricopper-polyoxometalate Catalysts for Water Oxidation: Redox-inertness of Copper Center. *J. Catal.* **2020,** *381*, 402-407; c) Martin-Sabi, M.; Soriano-López, J.; Winter, R. S.; Chen, J.-J.; Vilà-Nadal, L.; Long, D.-L.; Galán-Mascarós, J. R.; Cronin, L. Redox Tuning the Weakley-type Polyoxometalate Archetype for the Oxygen Evolution Reaction. *Nat. Catal.* **2018,** *1*, 208-213.
10. a) Du, J.; Lang, Z.-L.; Ma, Y.-Y.; Tan, H.-Q.; Liu, B.-L.; Wang, Y.-H.; Kang, Z.-H.; Li, Y.-G. Polyoxometalate-based Electron Transfer Modulation for Efficient Electrocatalytic Carbon Dioxide Reduction. *Chem. Sci*. **2020,** *11*, 3007-3015; b) Streb, C. New Trends in Polyoxometalate Photoredox Chemistry: from Photosensitisation to Water Oxidation Catalysis. *Dalton Trans* **2012,** *41*, 1651-1659; c) Majid, T.; Elaheh, M.; Amirhossein, T. Polyoxometalate as an Effective Catalyst for the Oxidative Desulfurization of Liquid Fuels: a Critical Review. *Rev. Chem. Eng*. **2019,** *36*, 831–858; d) Liu, S.-M.; Zhang, Z.; Li, X.; Jia, H.; Ren, M.; Liu, S. Ti-substituted Keggin-type Polyoxotungstate as Proton and Electron Reservoir Encaged into Metal-organic Framework for Carbon Dioxide Photoreduction. *Adv. Mater. Interfaces* **2018,** *5*, 1801062.
11. Ettedgui, J.; Diskin-Posner, Y.; Weiner, L.; Neumann, R. Photoreduction of Carbon Dioxide to Carbon Monoxide with Hydrogen Catalyzed by a Rhenium(I) Phenanthroline-polyoxometalate Hybrid Complex. *J. Am. Chem. Soc.* **2011,** *133*, 188-190.
12. Guo, W.; Lv, H.; Chen, Z.; Sullivan, K. P.; Lauinger, S. M.; Chi, Y.; Sumliner, J. M.; Lian, T.; Hill, C. L. Self-assembly of Polyoxometalates, Pt Nanoparticles and Metal-organic Frameworks into a Hybrid Material for Synergistic Hydrogen Evolution. *J. Mater. Chem. A* **2016,** *4*, 5952-5957.
13. a) Kuriki, R.; Sekizawa, K.; Ishitani, O.; Maeda, K. Visible-light-driven CO_2 Reduction with Carbon Nitride: Enhancing the Activity of Ruthenium Catalysts. *Angew. Chem. Int. Ed.* **2015,** *54*, 2406-2409; b) Kuriki, R.; Matsunaga, H.; Nakashima, T.; Wada, K.; Yamakata, A.; Ishitani, O.; Maeda, K. Nature-inspired, Highly Durable CO_2 Reduction System Consisting of a Binuclear Ruthenium(II) Complex and an Organic Semiconductor Using Visible Light. *J. Am. Chem. Soc*. **2016,** *138*, 5159-5170; c) Kuriki, R.; Yamamoto, M.; Higuchi, K.; Yamamoto, Y.; Akatsuka, M.; Lu, D.; Yagi, S.; Yoshida, T.; Ishitani, O.; Maeda, K. Robust Binding between Carbon Nitride Nanosheets and a Binuclear Ruthenium(II) Complex Enabling Durable, Selective CO_2 Reduction Under Visible Light in Aqueous Solution. *Angew. Chem. Int. Ed*. **2017,** *56*, 4867-4871.
14. a) Sato, S.; Matubara, Y.; Koike, K.; Falkenström, M.; Katayama, T.; Ishibashi, Y.; Miyasaka, H.; Taniguchi, S.; Chosrowjan, H.; Mataga, N.; Fukazawa, N.; Koshihara, S.; Onda, K.; Ishitani, O. Photochemistry of *fac*-[Re(bpy)$(CO)_3$Cl]. *Chem. Eur. J.* **2012,** *18*, 15722-15734; b) Kou, Y.; Nabetani, Y.; Masui, D.; Shimada, T.; Takagi, S.; Tachibana, H.; Inoue, H. Direct Detection of Key Reaction Intermediates in Photochemical CO_2 Reduction Sensitized by a Rhenium Bipyridine Complex. *J. Am. Chem. Soc.* **2014,** *136*, 6021-6030.
15. Schneider, T. W.; Angeles-Boza, A. M. Competitive ^{13}C and ^{18}O Kinetic Isotope Effects on CO_2 Reduction Catalyzed by Re(bpy)$(CO)_3$Cl. *Dalton Trans* **2015,** *44*, 8784-8787.
16. a) Jiang, Y.; Blacque, O.; Fox, T.; Berke, H. Catalytic CO_2 Activation Assisted by Rhenium Hydride/$B(C_6F_5)_3$ Frustrated Lewis Pairs-metal Hydrides Functioning as FLP Bases. *J. Am. Chem. Soc*. **2013,** *135*, 7751-7760; b) Benson, E. E.; Grice, K. A.; Smieja, J. M.; Kubiak, C. P. Structural and Spectroscopic Studies of Reduced $[Re(bpy\text{-}R)(CO)_3]^{-1}$ Species Relevant to CO_2 Reduction. *Polyhedron* **2013,** *58*, 229-234; c) Riplinger, C.; Carter, E. A. Influence of Weak Brønsted Acids on Electrocatalytic CO_2 Reduction by Manganese and Rhenium Bipyridine Catalysts. *ACS Catal.* **2015,** *5*, 900-908; d) Hayashi, Y.; Kita, S.; Brunschwig, B. S.; Fujita, E. Involvement of a Binuclear Species with the Re-C(O)O-Re Moiety in CO_2 Reduction Catalyzed by Tricarbonyl Rhenium(I) Complexes with Diimine Ligands: Strikingly Slow Formation of the Re-Re and Re-C(O)O-Re Species from Re(dmb)$(CO)_3$S (dmb = 4,4‘-Dimethyl-2,2‘-bipyridine, S = Solvent). *J. Am. Chem. Soc*. **2003,** *125*, 11976-11987; e) Riplinger, C.; Sampson, M. D.; Ritzmann, A. M.; Kubiak, C. P.; Carter, E. A. Mechanistic Contrasts between Manganese and Rhenium

Bipyridine Electrocatalysts for the Reduction of Carbon Dioxide. *J. Am. Chem. Soc.* **2014,** *136*, 16285-16298.

17. Frisch, M. J.; Trucks, G. W.; Schlegel, H. B.; Scuseria, G. E.; Robb, M. A.; Cheeseman, J. R.; Scalmani, G.; Barone, V.; Petersson, G. A.; Nakatsuji, H.; Li, X.; Caricato, M.; Marenich, A. V.; Bloino, J.; Janesko, B. G.; Gomperts, R.; Mennucci, B.; Hratchian, H. P.; Ortiz, J. V.; Izmaylov, A. F.; Sonnenberg, J. L.; Williams; Ding, F.; Lipparini, F.; Egidi, F.; Goings, J.; Peng, B.; Petrone, A.; Henderson, T.; Ranasinghe, D.; Zakrzewski, V. G.; Gao, J.; Rega, N.; Zheng, G.; Liang, W.; Hada, M.; Ehara, M.; Toyota, K.; Fukuda, R.; Hasegawa, J.; Ishida, M.; Nakajima, T.; Honda, Y.; Kitao, O.; Nakai, H.; Vreven, T.; Throssell, K.; Montgomery Jr., J. A.; Peralta, J. E.; Ogliaro, F.; Bearpark, M. J.; Heyd, J. J.; Brothers, E. N.; Kudin, K. N.; Staroverov, V. N.; Keith, T. A.; Kobayashi, R.; Normand, J.; Raghavachari, K.; Rendell, A. P.; Burant, J. C.; Iyengar, S. S.; Tomasi, J.; Cossi, M.; Millam, J. M.; Klene, M.; Adamo, C.; Cammi, R.; Ochterski, J. W.; Martin, R. L.; Morokuma, K.; Farkas, O.; Foresman, J. B.; Fox, D. J. *Gaussian 16, Revision A.03*, Wallingford, CT, 2016.
18. a) Vosko, S. H.; Wilk, L.; Nusair, M. Accurate Spin-dependent Electron Liquid Correlation Energies for Local Spin Density Calculations: a Critical Analysis. *Can. J. Phys.* **1980,** *58*, 1200-1211; b) Becke, A. D. Density-functional Exchange-energy Approximation with Correct Asymptotic Behavior. *Phys. Rev. A* **1988,** *38*, 3098-3100; c) Lee, C.; Yang, W.; Parr, R. G. Development of the Colle-Salvetti Correlation-energy Formula into a Functional of the Electron Density. *Phys. Rev. B* **1988,** *37*, 785-789; d) Becke, A. D. Density-functional Thermochemistry. III. The Role of Exact Exchange. *J. Chem. Phys.* **1993,** *98*, 5648-5652; e) Stephens, P. J.; Devlin, F. J.; Chabalowski, C. F.; Frisch, M. J. Ab Initio Calculation of Vibrational Absorption and Circular Dichroism Spectra Using Density Functional Force Fields. *J. Phys. Chem.* **1994,** *98*, 11623-11627.
19. a) Wadt, W. R.; Hay, P. J. Ab Initio Effective Core Potentials for Molecular Calculations. Potentials for Main Group Elements Na to Bi. *J. Chem. Phys.* **1985,** *82*, 284-298; b) Hay, P. J.; Wadt, W. R. Ab Initio Effective Core Potentials for Molecular Calculations. Potentials for K to Au Including the Outermost Core Orbitals. *J. Chem. Phys.* **1985,** *82*, 299-310; c) Hay, P. J.; Wadt, W. R. Ab Initio Effective Core Potentials for Molecular Calculations. Potentials for the Transition Metal Atoms Sc to Hg. *J. Chem. Phys.* **1985,** *82*, 270-283.
20. a) Tang, H.; Brothers, E. N.; Grapperhaus, C. A.; Hall, M. B. Electrocatalytic Hydrogen Evolution and Oxidation with Rhenium Tris(thiolate) Complexes: a Competition between Rhenium and Sulfur for Electrons and Protons. *ACS Catal.* **2020,** *10*, 3778-3789; b) Argibay-Otero, S.; Graña, A. M.; Carballo, R.; Vázquez-López, E. M. Synthesis of Novel Dinuclear N-Substituted 4-(Dimethylamino)benzaldehyde Thiosemicarbazonates of Rhenium(I): Formation of Four- and/or Five-Membered Chelate Rings, Conformational Analysis, and Reactivity. *Inorg. Chem.* **2020,** *59*, 14101-14117; c) Marazzi, M.; Gattuso, H.; Fumanal, M.; Daniel, C.; Monari, A. Charge-Transfer versus Charge-Separated Triplet Excited States of $[Re^{I}(dmp)(CO)_3(His124)(Trp122)]^+$ in Water and in Modified Pseudomonas aeruginosa Azurin Protein. *Chem. Eur. J.* **2019,** *25*, 2519-2526; d) Popov, D. A.; Luna, J. M.; Orchanian, N. M.; Haiges, R.; Downes, C. A.; Marinescu, S. C. A 2,2′-bipyridine-containing Covalent Organic Framework Bearing Rhenium(i) Tricarbonyl Moieties for CO_2 Reduction. *Dalton Trans* **2018,** *47*, 17450-17460.
21. a) Ditchfield, R.; Hehre, W. J.; Pople, J. A. Self-consistent Molecular-orbital Methods. IX. An Extended Gaussian-type Basis for Molecular-orbital Studies of Organic Molecules. *J. Chem. Phys.* **1971,** *54*, 724-728; b) Hehre, W. J.; Ditchfield, R.; Pople, J. A. Self-consistent Molecular-orbital Methods. XII. Further Extensions of Gaussian-type Basis Sets for Use in Molecular-orbital Studies of Organic Molecules. *J. Chem. Phys.* **1972,** *56*, 2257-2261; c) Hehre, W. J.; Pople, J. A. Self-consistent Molecular-orbital Methods. XIII. An Extended Gaussian-type Basis for Boron. *J. Chem. Phys.* **1972,** *56*, 4233-4234; d) Binkley, J. S.; Pople, J. A. Self-consistent Molecular-orbital Methods. XIX. Split-valence Gaussian-type Basis Sets for Beryllium. *J. Chem. Phys.* **1977,** *66*, 879-880; e) Francl, M. M.; Pietro, W. J.; Hehre, W. J.; Binkley, J. S.; Gordon, M. S.; DeFrees, D. J.; Pople, J. A. Self-consistent Molecular-orbital Methods. XXIII. A Polarization-type Basis Set for Second-row Elements. *J. Chem. Phys.* **1982,** *77*, 3654-3665.
22. a) Casida, M. E.; Jamorski, C.; Casida, K. C.; Salahub, D. R. Molecular Excitation Energies to High-lying Bound States from Time-dependent Density-functional Response Theory: Characterization and Correction of the Time-dependent Local Density Approximation Ionization Threshold. *J. Chem. Phys.* **1998,** *108*, 4439-4449; b) Stratmann, R. E.; Scuseria, G. E.; Frisch, M. J. An Efficient Implementation of Time-dependent Density-functional Theory for the Calculation of Excitation Energies of Large Molecules. *J. Chem. Phys.* **1998,** *109*, 8218-8224.
23. Zhao, Y.; Truhlar, D. G. The M06 Suite of Density Functionals for Main Group Thermochemistry, Thermochemical Kinetics, Noncovalent Interactions, Excited States, and Transition Elements: Two New Functionals and Systematic Testing of Four M06-class Functionals and 12 Other Functionals. *Theor. Chem. Acc.* **2008,** *120*, 215-241.
24. Handy, N. C.; Cohen, A. J. A Dynamical Correlation Functional. *J. Chem. Phys.* **2002,** *116* (13), 5411-5418.
25. Yanai, T.; Tew, D. P.; Handy, N. C. A New Hybrid Exchange-correlation Functional Using the Coulomb-attenuating Method (CAM-B3LYP). *Chem. Phys. Lett.* **2004,** *393*, 51-57.
26. Cancès, E.; Mennucci, B.; Tomasi, J. A New Integral Equation Formalism for the Polarizable Continuum Model: Theoretical Background and Applications to Isotropic and Anisotropic Dielectrics. *J. Chem. Phys.* **1997,** *107*, 3032-3041.
27. a) Aquilante, F.; Autschbach, J.; Baiardi, A.; Battaglia, S.; Borin, V. A.; Chibotaru, L. F.; Conti, I.; Vico, L. D.; Delcey, M.; Galván, I. F.; Ferré, N.; Freitag, L.; Garavelli, M.; Gong, X.; Knecht, S.; Larsson, E. D.; Lindh, R.; Lundberg, M.; Malmqvist, P. Å.; Nenov, A.; Norell, J.; Odelius, M.; Olivucci, M.; Pedersen, T. B.; Pedraza-González, L.; Phung, Q. M.; Pierloot, K.; Reiher, M.; Schapiro, I.; Segarra-Martí, J.; Segatta, F.; Seijo, L.; Sen, S.; Sergentu, D.-C.; Stein, C. J.; Ungur, L.; Vacher, M.; Valentini, A.; Veryazov, V. Modern Quantum Chemistry with [Open]Molcas. *J. Chem. Phys.* **2020,** *152*, 214117; b) Fdez. Galván, I.; Vacher, M.; Alavi, A.; Angeli, C.; Aquilante, F.; Autschbach, J.; Bao, J. J.; Bokarev, S. I.; Bogdanov, N. A.; Carlson, R. K.; Chibotaru, L. F.; Creutzberg, J.; Dattani, N.; Delcey, M. G.; Dong, S. S.; Dreuw, A.; Freitag, L.; Frutos, L. M.; Gagliardi, L.; Gendron, F.; Giussani, A.; González, L.; Grell, G.; Guo, M.; Hoyer, C. E.; Johansson, M.; Keller, S.; Knecht, S.; Kovačević, G.; Källman, E.; Li Manni, G.; Lundberg, M.; Ma, Y.; Mai, S.; Malhado, J. P.; Malmqvist, P. Å.; Marquetand, P.; Mewes, S. A.; Norell, J.; Olivucci, M.; Oppel, M.; Phung, Q. M.; Pierloot, K.; Plasser, F.; Reiher, M.; Sand, A. M.; Schapiro, I.; Sharma, P.; Stein, C. J.; Sørensen, L. K.; Truhlar, D. G.; Ugandi, M.; Ungur, L.; Valentini, A.; Vancoillie, S.; Veryazov, V.; Weser, O.; Wesołowski, T. A.; Widmark, P.-O.; Wouters, S.; Zech, A.; Zobel, J. P.; Lindh, R. OpenMolcas: from Source Code to Insight. *J. Chem. Theory Comput.* **2019,** *15*, 5925-5964.
28. Roos, B. O.; Veryazov, V.; Widmark, P.-O. Relativistic Atomic Natural Orbital Type Basis Sets for the Alkaline and Alkaline-earth Atoms Applied to the Ground-state Potentials for the Corresponding Dimers. *Theor. Chem. Acc.* **2004,** *111*, 345-351.
29. Marenich, A. V.; Ho, J.; Coote, M. L.; Cramer, C. J.; Truhlar, D. G. Computational Electrochemistry: Prediction of Liquid-phase Reduction Potentials. *Phys. Chem. Chem. Phys.* **2014,** *16*, 15068-15106.
30. Álvarez-Moreno, M.; de Graaf, C.; López, N.; Maseras, F.; Poblet, J. M.; Bo, C. Managing the Computational Chemistry Big Data Problem: The ioChem-BD Platform. *J. Chem. Inf. Model.* **2015,** *55*, 95-103.

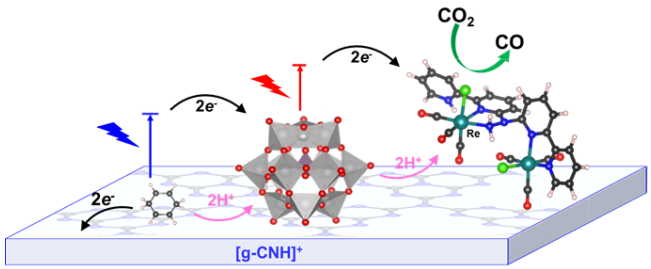
CO2
CO
2e-
2e-
2e-
2H+
2H+
Re
[g-CNH]+